Available online at www.sciencedirect.com

jmr&t
Journal of Materials Research and Technology
www.jmrt.com.br

Original Article

Simulation and experimental study of underwater dissimilar friction-stir welding between aluminium and steel

Arameh Eyvazian[a], *Abdelmagid Hamouda*[a], *Faris Tarlochan*[a], *Hamed Aghajani Derazkola*[b,*], *Farzad Khodabakhshi*[c,*]

[a] *Department of Mechanical and Industrial Engineering, Qatar University, Doha, Qatar*
[b] *Young Researchers and Elites Club, Science and Research Branch,Islamic Azad University, Tehran, Iran*
[c] *School of Metallurgy and Materials Engineering, College of Engineering, University of Tehran, P.O. Box: 11155-4563, Tehran, Iran*

ARTICLE INFO

Article history:
Received 29 November 2019
Accepted 1 February 2020
Available online 18 February 2020

Keywords:
Underwater friction-stir welding (FSW)
Volume of fluid (VOF) modeling
Aluminum
Steel
Microstructure
Mechanical property

ABSTRACT

The volume of fluid (VOF) modeling method was implemented to simulate the underwater friction-stir welding (FSW) process for dissimilar joining between aluminum and steel. Temperature profile, materials flow, and intermixing during dissimilar bonding under the cooling medium were monitored via VOF modeling and verified according to experimental data. The effects of processing parameters on the formation of intermetallic compounds (IMCs) at the Al/St interface, microstructural characteristics, and mechanical property of dissimilar weldments were studied and addressed. By decreasing tool rotational speed (w), increasing traverse velocity (v), and employing cooling medium, peak temperature continuously reduced (down to ~473 and 573 K for the aluminum and steel sides, respectively) led to substantial refining the grain structure and formation of a thinner IMC layer. The average grain size in the aluminum and steel sides of SZ is refined down to ~4 and 12 μm, respectively. The thickness of the IMC layer varied depending on the processing parameters with the lowest value of ~0.2 μm. The formation of a curved interface due to enhanced materials mixing at the advancing side is noted with a linear hardness gradient across the dissimilar weldment. Superior mechanical strength of ~80 MPa attained at an optimized submerged condition of w = 1650 rpm/v = 40 mm/min showed combined ductile-brittle fractographic aspects on the fracture surface.

© 2020 The Authors. Published by Elsevier B.V. This is an open access article under the CC BY-NC-ND license (http://creativecommons.org/licenses/by-nc-nd/4.0/).

* *Corresponding authors.*
E-mails: hamed.aghajani@srbiau.ac.ir (H.A. Derazkola), fkhodabakhshi@ut.ac.ir (F. Khodabakhshi).
https://doi.org/10.1016/j.jmrt.2020.02.003
2238-7854/© 2020 The Authors. Published by Elsevier B.V. This is an open access article under the CC BY-NC-ND license (http://creativecommons.org/licenses/by-nc-nd/4.0/).

1. Introduction

Newly, production of higher efficiency and low weight constructions encourage engineers for the production of hybrid structures. Among the various types of hybrid structures, dissimilar metallic structures are more notable due to the wide ranges of applications that can be serviced for different industries [1]. Steel (St)-aluminium (Al) dissimilar compound is one of the outstanding structures which considered by many automobile, aero, marine, and railway industries [2,3]. A well-known technique to manufacture the Al/St bi-metallic structure and combining properties of different parts is welding and joining processes. However, due to the large dissimilarity of physical and mechanical properties between dissimilar base materials and formation of intermetallics, dissimilar bonding between aluminum and steel is very challenging [4]. The presence of the brittle IMC layer at the Al/St interface can considerably deteriorate the mechanical performance of dissimilar weldments. On the other side, friction stir welding (FSW) is a promising, rapidly growing, and environmental friendly joining method that offers the great capability to join dissimilar materials with entirely different properties [5–11]. Therefore, this FSW route was implemented as a new solid-state joining technology to decrease the thickness of the IMC layer at the Al/St interface and improve the mechanical property of dissimilar weldments [12]. FSW displayed great flexibility for the production of different kinds of Al/St hybrid structures [13].

Submerged friction-stir welding under cooling mediums, such as compressed air, water, dry ice, and liquid nitrogen, can be considered as an alternate route of the standard solid-state technology for production of similar and dissimilar weldments from various metals and alloys [14]. In this new modification by submerging under the cooling atmosphere, it would be possible to control the solid-state metallurgical phenomena [15]. Considering the adiabatic nature of frictional heating during FSW treatment, the occurrence of joining process cannot affect by the cooling atmosphere [16,17]. However, immersing under the cooling medium can affect the extend of cooling rate after FSW from the peak down to room temperature and subsequent metallurgical reactions [18]. By controlling the frequency of grain growth after dynamic restoration phenomena in the stirred area as well as the intermetallic compounds (IMCs) formation, the submerged cooling atmosphere can induce different mechanical properties during FSW treatment of various metals and alloys [14,19–21]. In this regard, the formation of a nano-sized cellular structure with the average size of ~20 nm in aluminum matrix was reported in the research by Khodabakhshi et al. [14] on friction-stirring of metal-matrix nanocomposites. Although several kinds of research were reported in the literature on the context of similar and dissimilar FSW joining for different metals and alloys, meanwhile, the limited results reported on submerged FSW treatment.

Underwater friction-stir welding (UFSW) firstly employed for similar joining of metals and alloys with the main object of refining the grain structure of weld nugget to improve the mechanical strength of weldment. In the reports of Zhang and Liu [22–29], the implementation of the UFSW process led to enhancement of the tensile strength of AA2219 aluminum alloy around ~80%. Sabari et al. [30,31] showed that by controlling the UFSW parameters, the size of the thermo-mechanical affected zone (TMAZ) and heat-affected zone (HAZ) could be minimized in the joint line of AA2519-T87 aluminum alloy. Heirani et al. [32] studied the UFSW process for welding of AA5083 aluminum alloy. They showed that it has a drastic influence on improving the hardness and tensile strength of weldment as compared to the air processing condition. Liang et al. [33] demonstrated that the mechanical strength of AA7055 aluminum alloy weldment after the UFSW process affected by change the water temperature. The results showed that using higher tool rotational speed at warm temperature-induced superior joint strength as compared to the cold and room temperature water conditions [34,35]. Papahn et al. [36] examined the UFSW treatment for AA7075-T6 aluminum alloy plates. They showed that the produced maximum temperature in the SZ decreased (close to 40%) as compared with the air-processing FSW. They have reported reducing the peak temperature of the stirred zone and increasing the cooling rate under the cooling medium as compared to the air processing condition led to more brittleness and higher strength of weldment. Tan et al. [37] showed that the size of recrystallized grains and the number of secondary phase particles in the SZ was reduced with decreasing the water temperature during UFSW of AA3003 aluminum alloy.

According to the current limited state of the art on dissimilar underwater friction-stir welding, impressive results were reported in the literature in some cases. Zhao et al. [38,39] highlighted the UFSW process as a valid route for dissimilar joining of AA6013 aluminum alloy and AZ31 magnesium alloy with a higher tensile strength (~152 MPa) as compared to the air processing condition (~131 MPa). They have also reported the formation of Al_3Mg_2 and $Mg_{17}Al_{12}$ phases at the interface between aluminum and steel after the UFSW process. In another report, Zhang et al. [40] worked on dissimilar UFSW joining between aluminum and copper, where the results showed reducing in the amount of Al/Cu intermetallic compounds under UFSW condition. Dropping the thickness of the IMC layer at the interface of AA6061-T6 aluminum alloy and AISI 304 steel was reported in the research of Mahto et al. [41] under the action of UFSW treatment. Accordingly, the thickness of the IMC layer was decreased from ~9.5 μm for reasonable FSW condition down to ~0.5 μm after UFSW with the considerable refinement of grain structure in the weld nugget and significant improvement of mechanical strength. Recently, Aghajani Derazkola and Khodabakhshi [15] investigated the dissimilar bonding between Al-Mg aluminum alloy and A441 AISI steel by the UFSW process under different water medium temperatures. They have reported the room temperature water as the optimum cooling medium with a maximum tensile strength of ~310 MPa and elongation of ~13%.

Despite these exciting but limited results on the context of UFSW dissimilar bonding between aluminum and steel, no reports were found in the literature of modeling results to simulate the influence of the submerged cooling medium on the characteristics of produced dissimilar weldments. Furthermore, the effects of UFSW processing parameters in terms of rotational speed of FSW tool and traverse velocity on the microstructural details and mechanical performance of dissimilar weldments were not addressed yet. Therefore, the

Table 1 – Chemical composition of base materials.

Element (wt%)	AA5182 Aluminum alloy	AISI 1010 Steel
Al	94	0
Fe	0.35	99.1
Cr	0.1	0
Mg	5.0	0
Mn	0.5	0.6
Si	0.2	0
Ti	0.1	0
Zn	0.25	0
C	0	0.13
P	0	0.04
S	0	0.13

Table 2 – Physical and mechanical properties of base materials.

Properties	AA5182 Aluminum alloy	AISI 1010 Steel
Density	2780 kg/m^3	7870 kg/m^3
Ultimate tensile strength (UTS)	275 MPa	365 MPa
Yield tensile strength	103 MPa	305 MPa
Elongation at break	21%	20%
Vickers hardness	84	108
Shear strength	150 MPa	240 MPa
Thermal conductivity	126 W/m-K	49.8 W/m-K
Melting point	638 °C	1516 °C

Table 3 – The UFSW processing parameters.

Sample number	Tool rotational velocity (rpm)	Tool traverse velocity (mm/min)
I	950	40
II	950	70
III	950	100
IV	1300	40
V	1300	70
VI	1300	100
VII	1650	40
VIII	1650	70
IX	1650	100
X	2000	40
XI	2000	70
XII	2000	100

main object of this research is to introduce an advanced numerical model for predicting the characteristics of UFSW process. In the following, the simulation results were validated according to the experimental results by UFSW joining on the hybrid structures between AA5182 aluminum alloy and AISI 1010 steel under different processing conditions.

2. Experimental procedure

The rectangular $8 \times 200 \times 150\,mm^3$ pieces cross-sectioned using a universal sawing machine from the AA5182 aluminum alloy and AISI 1010 steel sheets. Chemical compositions and mechanical properties for these raw materials are presented in Tables 1 and 2, respectively. A Plexiglas surrounded set-up installed on a high energy milling machine to implement the UFSW process. The electronic macro-image from the employed set-up for the accomplishment of the UFSW process is illustrated in Fig. 1 The temperature of the water medium was controlled around 298 K during all experiments. An FSW tool was utilized made of tungsten carbide (WC) with a shoulder diameter of 20 mm containing a treated frustum probe with a conical bore in the range of 10 to 6 mm and a length of 7.6 mm. During UFSW tests, the tool tilting angle was preserved constantly about 2 degrees with a continual plunge depth of 0.4 mm. The employed processing parameters in terms of rotational speed (w) and traverse velocity (v) for UFSW treatment are presented in Table 3. Three K-type thermocouples (Omega, USA) were inserted at locations with 10, 14, and 18 mm distances from the interface edge of base metals, as shown in Fig. 1. For studying the microstructural evolutions, dissimilar weldments were cross-sectioned perpendicular to the FSW direction by a

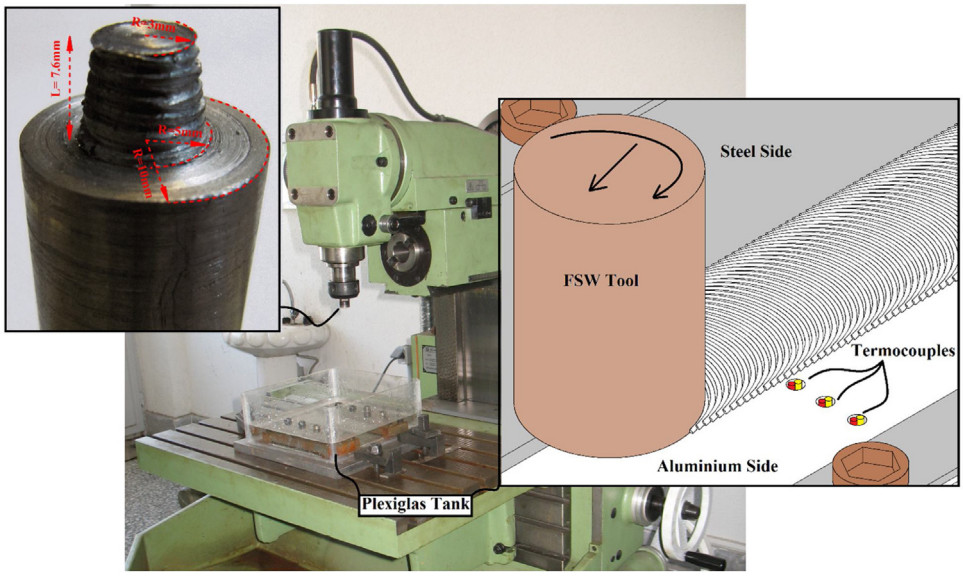

Fig. 1 – The utilized UFSW set-up.

diamond cutter, grounded on the SiC emery papers, and polished on the diamond pastes. After standard metallographic sample preparation, the grain structure of different regions across dissimilar weldments from aluminum and steel sides revealed using modified Poulton's and Nital's reagents, respectively. For microstructural observations, an optical microscope (VERSAMET-3, USA) was used as equipped with an image analyzing software (Clemex-Vision, USA). To study the materials flow pattern as well as the intermetallic compounds (IMCs) formation across the dissimilar weldments, a field-emission scanning electron microscope (VEGA//TESCAN-XMU SEM, RUSSIA) equipped with an energy dispersive X-ray spectroscopy (EDS) detector was utilized. To elaborate on the mechanical behavior of processed dissimilar weldments, tensile testing and indentation hardness measurements were performed. For tensile testing, coupons were prepared according to the ASTM E8-M03 Standard with a gauge length of 32 mm. Under each processing condition, tensile testing was repeated three times, and average values for tensile properties were calculated and reported. The fractographic aspects on the fracture surface of tensile failed samples were studied under SEM analysis. Vickers micro-hardness measurements were performed using an HMV-2 T Shimadzu Model Micro-Indenter and hardness profiles reported.

3. Numerical modelling of UFSW process

3.1. Assumptions

The steady-state stage of the FSW process in the submerged condition was modeled, whereas materials flow into the computational domain varied in terms of welding speed. In the modeling procedure to simulate the dissimilar joining process, the FSW tool was considered at a fixed location with a specific tool rotational speed and plasticized material moved around the rotating device. For this purpose, base materials were considered as the non-Newtonian fluids with high viscosity. A laminar regime estimated the flow field of fluids, and the coherence varied as a function of temperature and strain rate. In this context, the volume of fluid (VOF) method was employed to simulate the underwater friction stir welding (UFSW) process. Aluminum alloy and steel were considered for treatment as different phases during the UFSW process. Due to the micro-scale formation of intermetallic compound (IMC) layers at the interface and small amount of steel particles as in the aluminum matrix, they were neglected in the modeling procedure for simplification.

3.2. Governing equations

As described before, in this modeling procedure, the dissimilar FSW process was defined as the separated multiple phase flow categories, and the dissimilar materials were not interpenetrated to each other. One of the popular methods to deal with such complex modeling problems is the VOF. According to this modeling approach, χ_k is introduced as a variable for volume fraction (phase distribution) of phase k to describe the phase distribution. Velocity (v), temperature (T), and pressure (P) fields are the shared parameters among the dissimilar

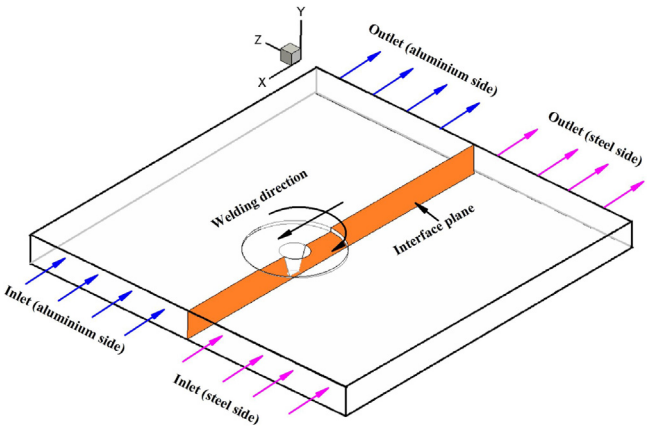

Fig. 2 – Schematic view of UFSW process modeling.

phases, and material properties can be considered as the averaged values based on the volume fraction χ_k in each unit cell. To determine the χ_k parameter and describe the dissimilar materials flow, the conservation relations for mass, momentum, and energy can be accordingly derived and solved as following [47–49]:

$$\text{Mass}: \ \tilde{\nabla}.\left(\chi_k\rho_k\tilde{v}\right) = \sum_{j=1}^{2}\left(\dot{m}_{jk} - \dot{m}_{kj}\right) \tag{1}$$

$$\text{Momentum}: \ \tilde{\nabla}.\left(S\tilde{v}\tilde{v}\right) = -\tilde{\nabla}P + \tilde{\nabla}.\Gamma \tag{2}$$

$$\text{Energy}: \ \tilde{\nabla}.\left[\left(\sum \chi_k\rho_k c_k\right)T\tilde{v}\right] = -\tilde{\nabla}.\tilde{\bar{q}} + \tilde{\nabla}.\left[\left(\Gamma - p\tilde{I}\right).\tilde{v}\right] \tag{3}$$

where $\tilde{\nabla}$ is the special vector differential operator, ρ_k is the density of k phase, and $\tilde{v}$ is the velocity. The mass conservation equation is a function that determining the volume fraction of each phase in the different elements. The mass transfer rate from phase k to phase j can provide as $\dot{m}_{kj}$ and in the switched condition, it can be defined by $\dot{m}_{jk}$ parameter (see Fig. 2 and Appendix A for more details and settings).

3.3. Boundary conditions

The most critical boundary condition in the FSW process is the coupled thermal-mechanical interface between the workpiece and tool. The heat generated at the interface between the vertical and horizontal surfaces of the tool pin and the workpiece can be defined as following [42]:

$$Q_i = \left[(1-\delta)\,\eta\tau + \delta\mu_f P_N\right](\omega r - v_1\sin\theta)\,\frac{A_r}{F} \tag{4}$$

where A_r is a small area on the tool pin-workpiece interface, r is the radial distance of the area center from the tool axis, F is the control-volume enclosing the area A_r, τ is the maximum shear stress at yielding, θ is the angle with the negative x-axis in the counter-clockwise direction, η is the mechanical efficiency (the amount of mechanical energy converted to the heat energy), δ denotes the spatially variable fractional slip

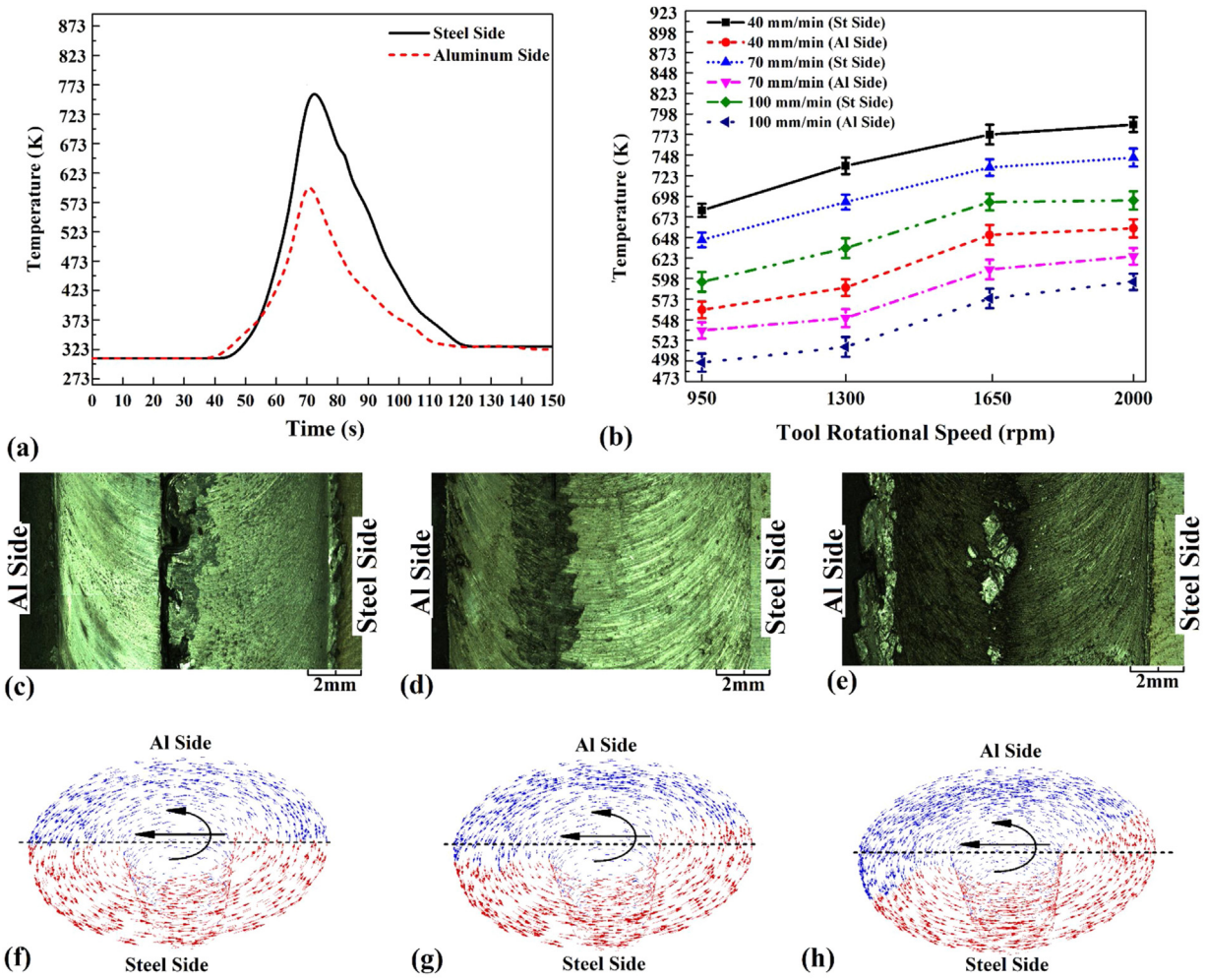

Fig. 3 – (a) The recorded temperature profile for Sample X. (b) Relation between recorded peak temperature and parameters of the UFSW process. Surface flow patterns of (c) Sample III, (d) Sample VII and (e) Sample X. VOF vector results for (f) Sample III, (g) Sample VII and (h) Sample X.

between the tool and the workpiece interface (which selected as 0.44), μ_f is the spatially variable coefficient of friction, ω is the angular velocity, and P_N is the average pressure on the surface (see Appendix B for more details and parameters). It is worth noting that FSW is a kind of high strain rate adiabatic severe shear deformation, and the primary influence of the cooling medium would be on controlling the rate of cooling from peak temperature down to atmosphere after treatment. The cooling water effect on the boundary conditions was considered in the modeling procedure. The relating details in terms of governing equations, as well as physical parameters and values, were expressed in two appendixes of A and B at the end of the manuscript in the form of "Supplementary Electronic Document".

4. Results and discussion

4.1. *Thermal history and surface material flow pattern*

Fig. 3a presents the recorded thermal cycles during the UFSW process from the aluminum and steel sides for Sample X. As expected, the maximum or peak temperature in the steel side is higher than the aluminum side due to higher melting temperature of steel rather than the aluminum as well as the higher strength, lower plasticity, less heat sinking capability, and lower thermal conductivity (see Table 2 in comparison between the physical and mechanical properties of AA5182 aluminum alloy and AISI 1010 steel). In Fig. 3b, the maximum or peak temperature is plotted as a function of rotational speed and traverse velocity for both aluminum and steel sides of dissimilar weldments. As shown, by increasing w and decreasing of v, the peak temperature is continuously increased due to the increasing heat input index in terms of expanding the w/v ratio. Under all processing conditions, the measured peak temperature for the steel side is higher than the aluminum one. According to these experimental results, the highest peak temperature is determined for the steel side of Sample X, and it is around 777 K. Meanwhile, the lowest temperature is ~498 K for the aluminum side of Sample III with the less heat generation at the minimum UFSW heat input index of $w = 950$ rpm and $v = 100$ mm/min. Based on the presented data in Fig. 3b, a correlation can be established between the maxi-

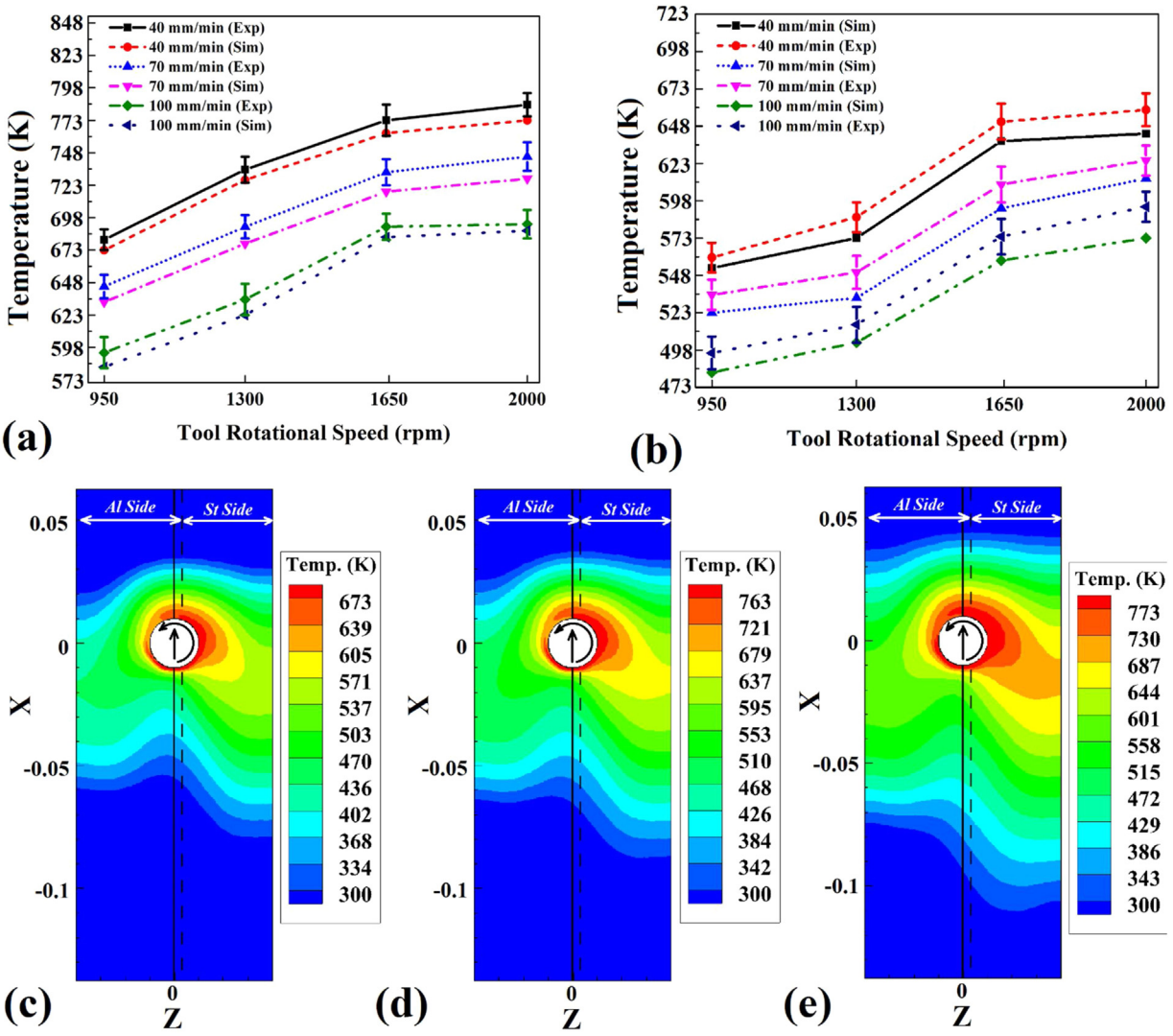

Fig. 4 – Simulation results for the maximum temperature in (a) the steel and (b) aluminum sides versus tool rotational speed and traverse velocity. Simulation results for the surface temperature distribution in (c) Sample III, (d) Sample VII and (e) Sample X.

mum temperature and tool velocity for the UFSW process. For thermal data in both Fig. 3(a and b), they are relating to the stirred region for the nearest point under the shoulder area.

Surface materials flow and materials dissimilar mixing for the surface of dissimilar weldments processed under the action of different UFSW parameters are demonstrated in Fig. 3(c–e). As it is well established, the significant influence of UFSW treatment as compared to air processing is the impact of the submerged cooling medium on affecting the heat transfer and cooling rate after the welding process. Therefore, for Sample III with the lowest heat input index ($w = 950$ rpm and $v = 100$ mm/min), the faulty materials flow and intermixing led the formation of a non-sound or defect-free dissimilar joint, as shown in Fig. 3c. By increasing the heat input index toward Samples VII and X in terms of increasing the tool rotation speed and decreasing the tool traverse velocity, the enhanced materials flow and uniform mixing can be noted. Under the high heat input index processing condition, for instance, in the case of Sample X, the formation of surface flash is depicted in the aluminum side of the dissimilar weldment, as shown in Fig. 3e. The simulation results as plots of the volume fraction vector for intermixing of aluminum and steel different metals in terms of changing the rotational speed and traverse velocity in the case of Samples III, VII, and X are presented in Fig. 3(f–h). According to these modeling predictions, the diffusion and mixing of aluminum into the steel side are mainly under the influence of the heat input index for the submerged underwater condition.

Fig. 4(a and b) show the variation of simulated peak temperature versus tool rotational speed and traverse velocity under the recorded temperature for both steel and aluminum sides, respectively. Based on these graphs, a good agreement between the simulation and experimental results can be noted. Although, the matching for the steel side seems closer with less error. In most processing conditions, the standard deviation range of experimental data can cover the simulation results, as well. It is worth noting that while the trends of the experimental and simulated peak temperatures are similar,

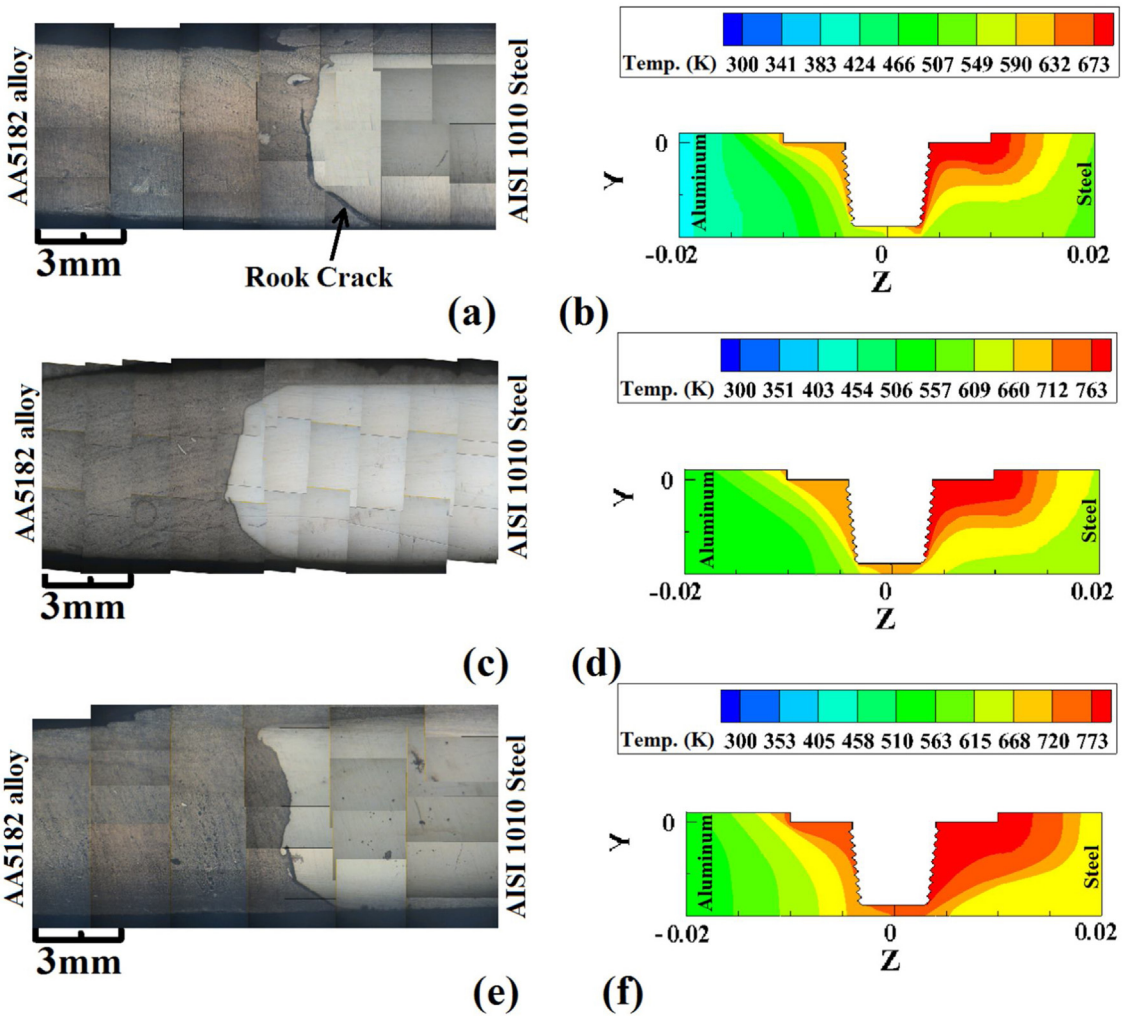

Fig. 5 – (a, c, e) Cross-sectional materials flow pattern view and (b, d, f) simulated results of internal temperature distribution for (a, b) Sample III, (c, d) Sample VII, and (e, f) Sample X.

the experimental one seems higher than the simulated one, it can be due to some assumptions in the modeling procedure, as described in Section 3. Furthermore, the simulations result in terms of the surface heat distribution or temperature contours are demonstrated in Fig. 4(c–e) in the case of Samples III, VII, and X. As shown and expected, the frictional heat generation in the steel side is more than the aluminum part. According to temperature profiles, the generation of temperature profiles is mainly focused and shifted toward the steel side due to the lower heat transfer coefficient of AISI steel as compared to the AA5183 aluminum alloy. In comparison between Fig. 4(c–e), it is evident that by increasing w and decreasing v, the region of experienced high peak temperature highlighted by red-color in the contours extended more toward the steel side.

4.2. *Internal materials flow*

In Fig. 5, the cross-sectional temperature profiles and material flow patterns for dissimilar aluminum-steel weldments processed under different UFSW parameters are demonstrated. In this regard, the optical macrographs from Samples III, VII, and X are presented, showing the alteration of rotational speed and traverse velocity. Accordingly, an excellent correlation can be established between the temperature profile and dissimilar materials intermixing. Less frictional heat generation under low tool rotational speed and high traverse velocity (low heat input index) lead insufficient different aluminum and steel materials intermixing in the case of Sample III which induced the formation of a root canal crack under the bead of dissimilar weldment across the interface, as shown in Fig. 5(a and b). However, by increasing the heat input index in terms of increasing the w or reducing the v, the materials intermixing across the interface between aluminum and steel and in following the formation of dissimilar weldment are enhanced. In the case of these two samples VII and X, as demonstrated in Fig. 5(c–f), dissimilar weldments seems sound with no formation of a macro-obvious welding defect. As seen, the shape or morphology of aluminum and steel interface is mostly affected by changing the UFSW processing parameters. It seems that by increasing the heat input index in terms of w/v ratio, the hard steel material becomes softer by increasing the

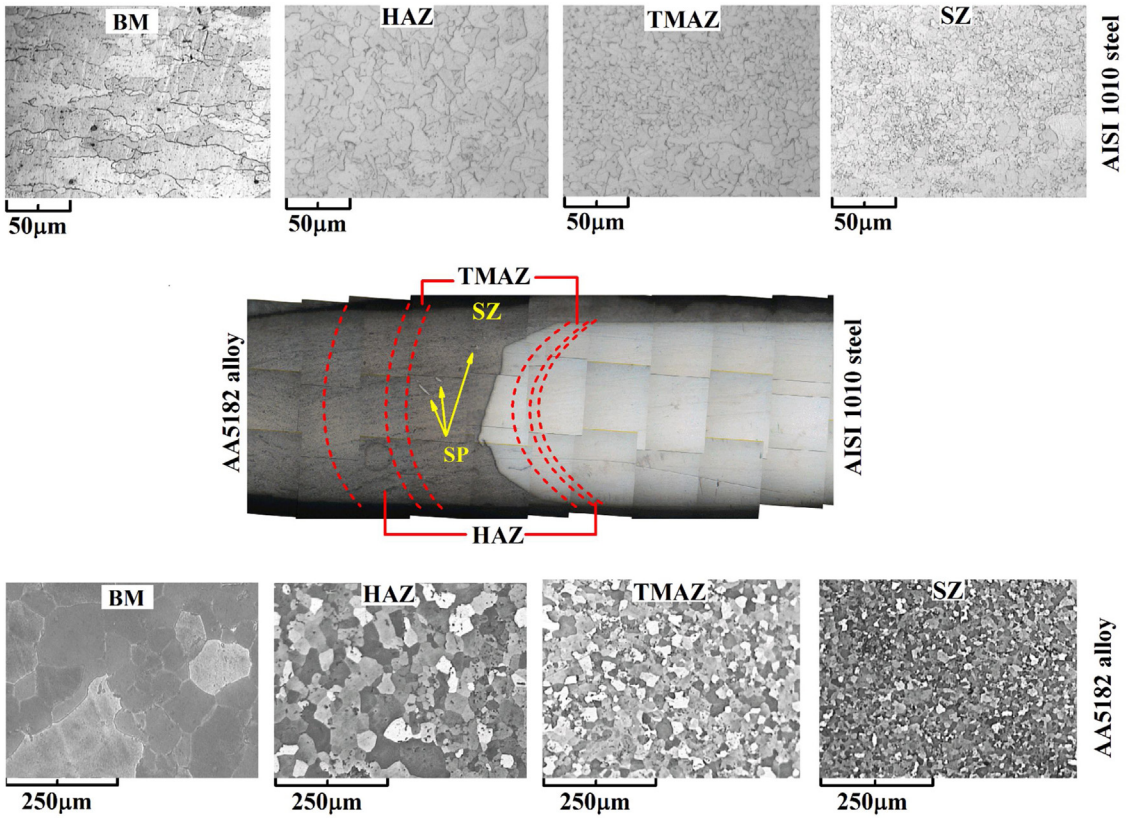

Fig. 6 – Optical images showing the microstructure of different regions across Sample VII.

peak temperature, which can make the materials flow and intermixing easier (see Fig. 5a,c,e). On the other side, simulation results for the internal heat distribution in Fig. 5(b,d,f) reveals by increasing w or decreasing v; the more heat can generate in the steel side led more stretching of steel toward the aluminum side.

4.3. *Microstructure of dissimilar weldments*

Fig. 6 illustrates the macro-image of a dissimilar weldment across the thickness section for Sample VII after UFSW treatment as combined with the optical microstructures of different regions. In this figure, the grain structure of all areas has the possibility of formation during the UFSW process is addressed for both aluminum and steel sides, as base metal (BM), heat affected zone (HAZ), thermo-mechanical affected zone (TMAZ), and stir zone (SZ). According to these presented results, the formation of a narrow HAZ and TMAZ regions can be noted for both aluminum and steel sides of dissimilar weldments under the UFSW processing conditions due to rapid cooling from peak temperature down to atmosphere. According to these microstructural maps, the grain structure in TMAZ and especially in the SZ region, is largely refined after UFSW treatment. The main controlling mechanisms for such grain structural modification are based on the operative dynamic restoration phenomena during the UFSW process [19,21,43,44]. The involved mechanisms mostly include dynamic recovery (DRV), continuous dynamic recrystallization (CDRX), discontinuous dynamic recrystallization (DDRX), and geometric dynamic recrystallization (GDRX) depending on the stacking fault energy of the examined metals and alloys [45]. As compared to the conventional FSW process, the main difference of UFSW treatment is utilizing the submerged medium. Since friction-stirring is an adiabatic process, the peak temperature inside SZ cannot affect by the submerged cooling medium. Meanwhile, after friction-stirring, the rate of cooling from peak temperature can be influenced mainly by the submerged cooling medium [43]. Grains can nucleate during severe plastic deformation of friction-stirring process, and in following rapid cooling from the peak temperature after the UFSW process will render the grain growth, and the rate of grain boundaries migration lead to the formation of a fine equiaxed grain structure in both aluminum and steel sides of dissimilar weld nugget. Some degree of grain coarsening in a narrow region of HAZ from the aluminum side can be observed. In the SZ of the steel side, a kind of bimodal grain structure consist of fine and coarse boundaries is seen. Although, the grain structure in TMAZ of both aluminum and steel sides seems directional due to induced frictional shear by rotating shoulder during UFSW treatment outside of SZ. Due to the rapid cooling of the UFSW process, no grain structural coarsening detected in the HAZ of the steel side. Fig. 6 only show the microstructural characterization results for one sample. The summary of microstructural analysis results for all samples is demonstrated in Fig. 7. For three regions of HAZ, TMAZ, and SZ, the average grain size for

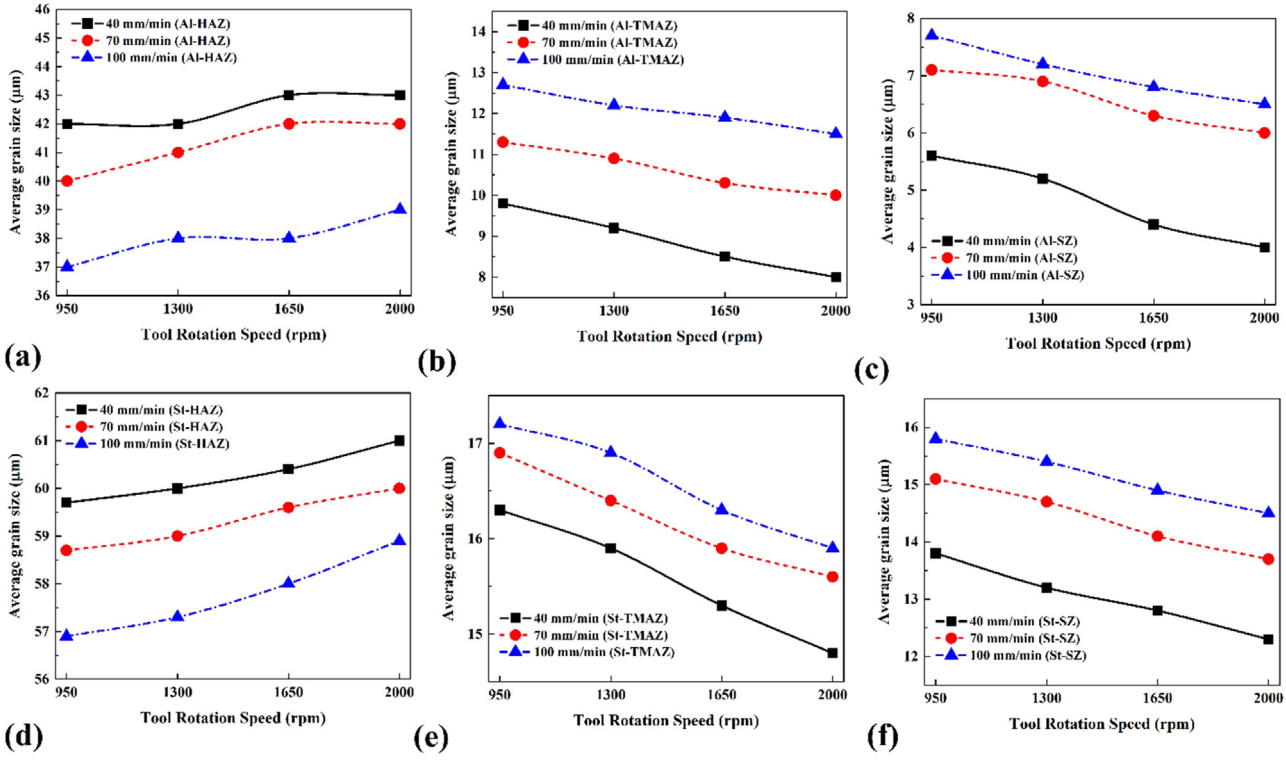

Fig. 7 – The relation between the average grain size and tool processing parameters for (a, d) HAZ, (b, e) TMAZ, and (c, f) SZ regions of (a–c) aluminum and (d–f) steel sides after UFSW.

both aluminum and steel sides are determined under different UFSW processing conditions and presented in Fig. 7(a–f). The influence of UFSW heat input on the average grain size alteration found opposite for the HAZ region as compared to TMAZ and SZ. In the HAZ area, by increasing w and decreasing v or increasing the heat input index in terms of w/v ratio, the average grain size is continuously increased for both aluminum and steel sides, as shown in Fig. 7(a and d), respectively. According to these results, the main controlling parameter on the grain structure of the HAZ area in both aluminum and steel sides is the tool traverse velocity. For both TMAZ and SZ regions, the heat input index ratio has opposite influence on the trend of average grain size versus the rotational speed and traverse velocity of tool, as shown in Fig. 7(b,c) and (e,f). In these regions, by increasing the w/v ratio, the average grain size is continuously refined. This observation is not agreement with the reported results regarding standard FSW treatment in the literature [46]. Since it is expected that higher heat input must lead the generation of coarser grain structure, meanwhile, under UFSW treatment by employing the water like a submerged cooling medium, the situation would be completely different. In this context, increasing w and reducing v can lead the formation of more nucleates due to inducing severe shear straining, and in following by controlling the rate of grain growth after rapid cooling during UFSW treatment, the finer grains can be formed. Under the extreme UFSW processing parameters, the formation of a fine equiaxed grain structure with the average size <4 μm and 12 μm can be noted for both aluminum and steel sides of dissimilar weldments (see Fig. 7c and f).

Table 4 – Chemical composition of the IMC layer at the upper area of dissimilar joints.

Sample	Fe (wt%)	Al (wt%)	Mg (wt%)
I	48.6	49	2
II	47.6	49.7	2.3
III	47.4	49.6	2.4
IV	46.5	51.5	1.5
V	43.8	54.3	1.7
VI	42.6	55.2	1.8
VII	44.4	53.7	1.3
VIII	42.6	55.6	1.4
IX	41.9	56.5	1.5
X	45.8	52.9	1.1
XI	43.7	54.8	1.2
XII	43.9	54.7	1.2

4.4. *Intermetallic compounds (IMCs) layer formation and growth*

FE-SEM micrographs from the aluminum and steel interface for upper and lower regions of dissimilar weldments processed under different conditions in the case of Samples III, VII, and X are demonstrated in Fig. 8a. Formation of a thin intermetallic compounds (IMCs) layer between aluminum and steel at the interface is noticeable. As can be found, the thickness and morphology of the IMC layer are largely varied for upper and lower regions of dissimilar weldments depending on the rotational speed and traverse velocity of tool. For all processing conditions, the thickness of the IMC layer at the top area is higher than the lower one caused by more senior tool

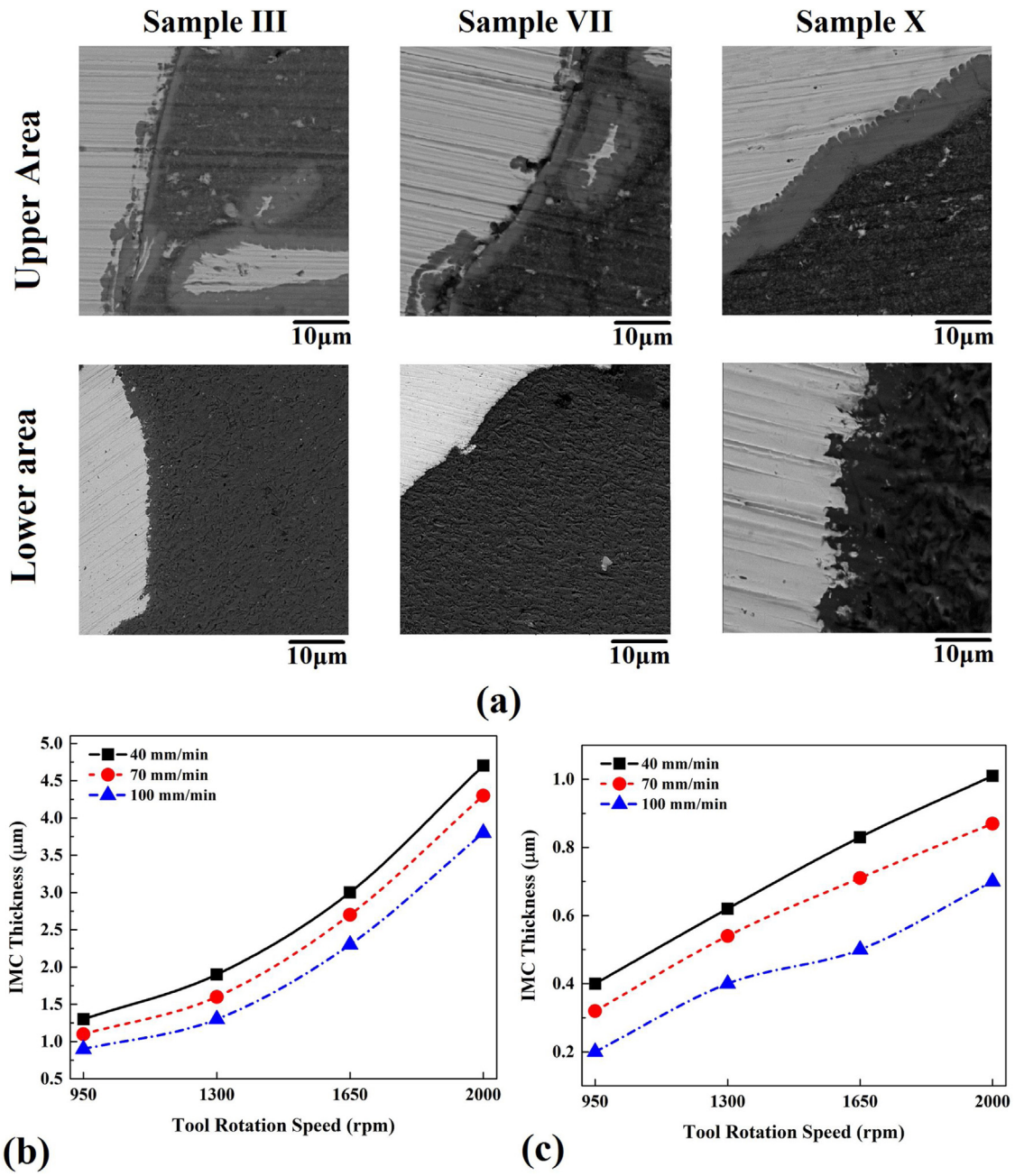

Fig. 8 – (a) SEM images showing the formation of IMC layer at the Al/St interface depending on the UFSW parameters across Samples III, VII, and X. Relation between the thickness of IMC layer and tool processing parameters for the (b) upper and (c) lower regions of dissimilar weldments.

frictional heating on the surface under the action of the rotating shoulder. Despite the thinner IMC layer for the smaller area of dissimilar weldments, the central fact was the formation of a wavy interface in that region under the influence of rotating pin led intensified mechanical interlocking. In the following, the thickness of the IMC layer formed at the interface is determined based on these FE-SEM images and plotted as a function of tool processing velocity for upper and lower parts of dissimilar weldments in Fig. 8(b and c), respectively. As seen, by increasing w and decreasing v, the thickness of the IMC layer after UFSW treatment is continuously increased with different trends for both different upper and lower regions of dissimilar joints. For instance, the depth of the IMC layer in the upper part for Sample III is ~0.6 μm (thinner one), which improved up to ~4.7 μm (thicker one) in the case of Sample X. As compared to the normal FSW joining of dissimilar aluminum and steel weldments reported in the literature before [46], the primary influence of the submerged cooling environment is on restricting the growth rate of the IMC layer by the action of rapid cooling from the peak temperature. Meanwhile, under a specific submerged cooling medium condition, higher processing heat input leads to the formation of a thicker IMC layer. According to EDS elemental mapping analysis results from the aluminum and steel interface illustrated in Fig. 9, the cooling

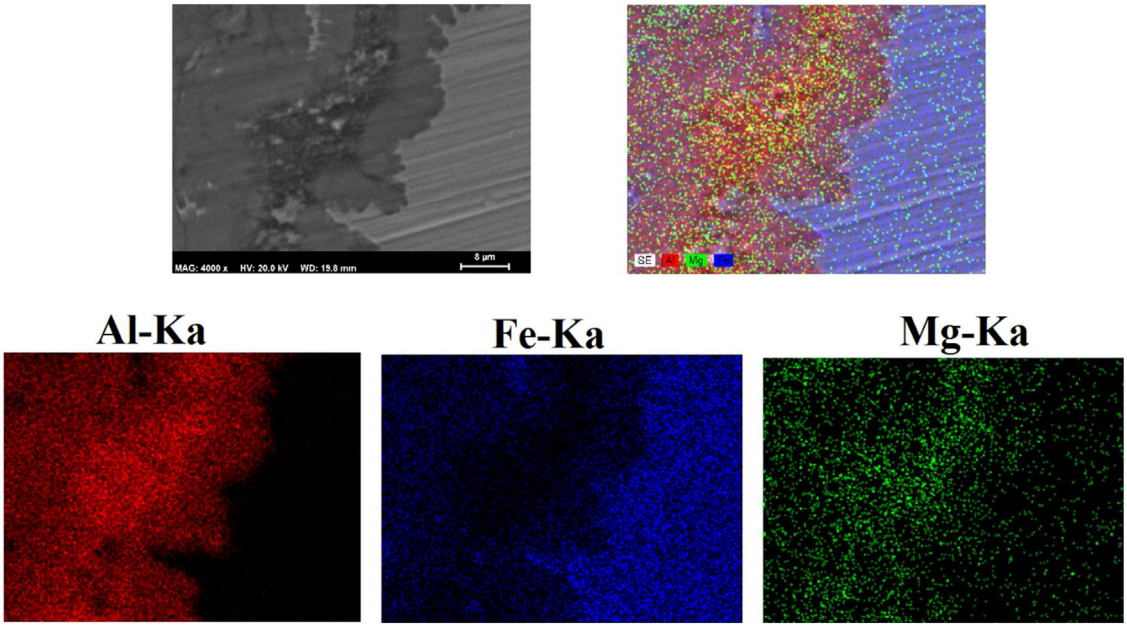

Fig. 9 – The EDS elemental map is showing the formation of the IMC layer from the upper area of Sample X.

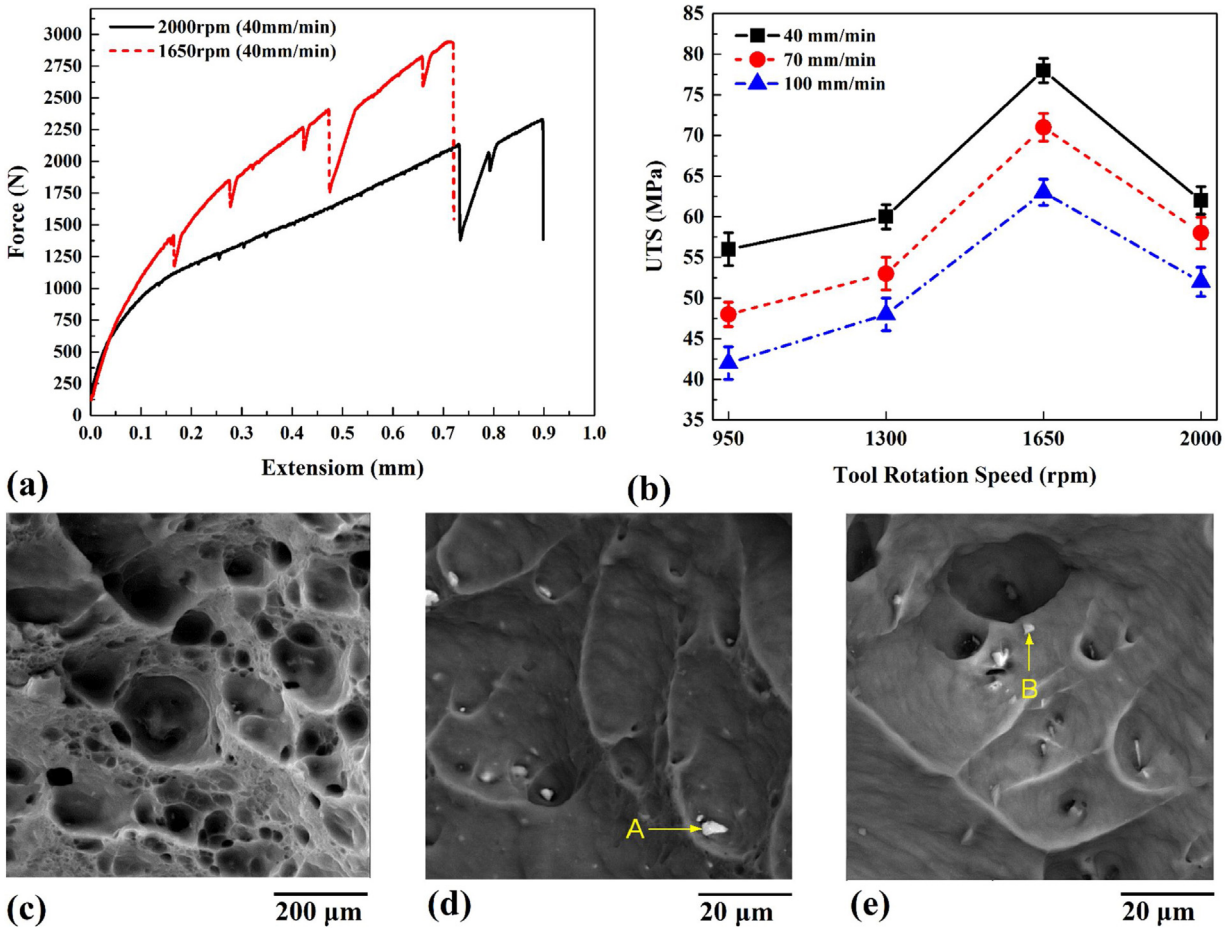

Fig. 10 – (a) Force-displacement graphs determined during transverse tensile testing of Samples VII and X. (b) Variations of UTS for dissimilar weldments versus rotational speed and traverse velocity. (c) Low magnification and (d, e) high magnification SEM images from the fracture surface of sample X.

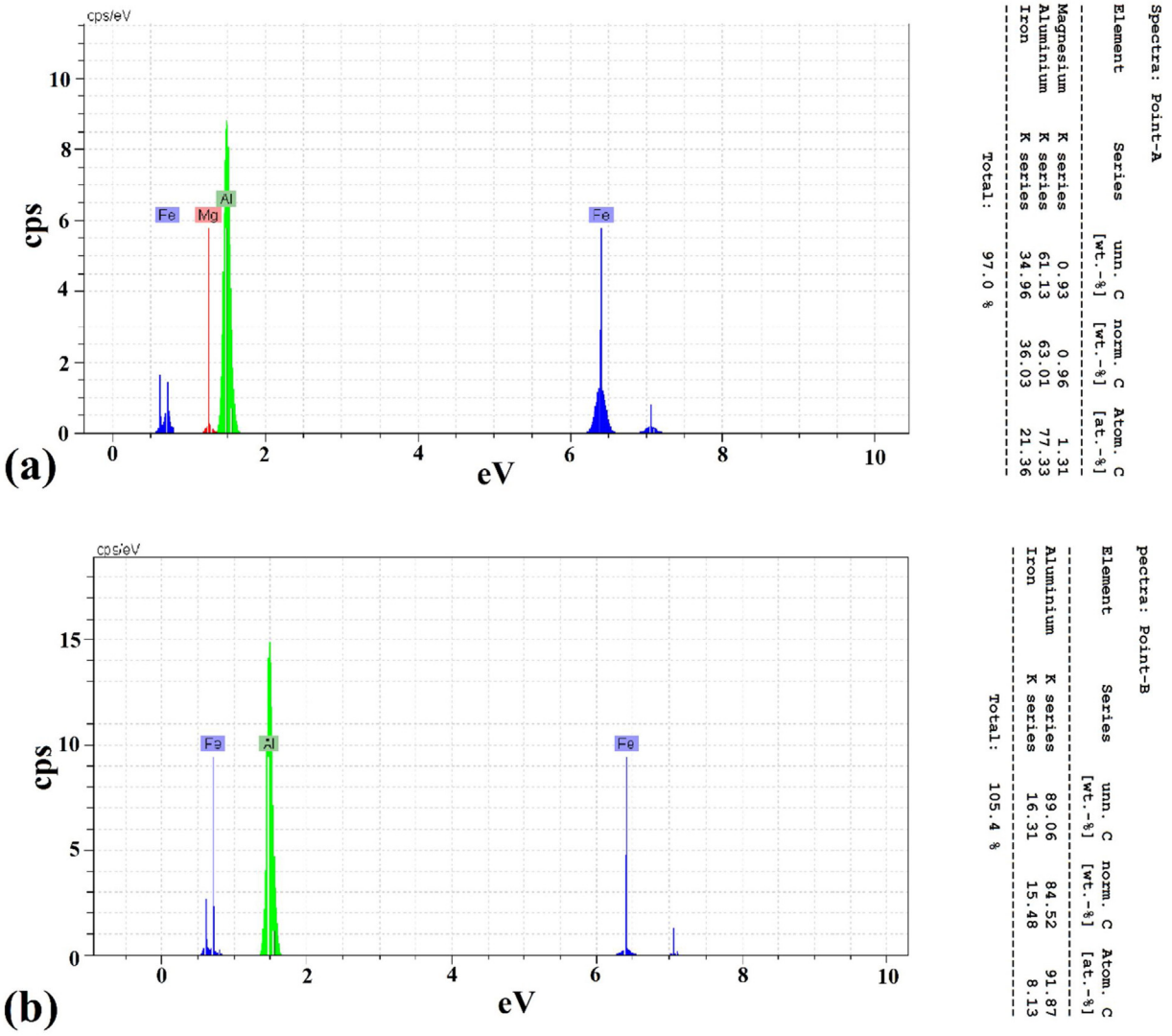

Fig. 11 – The EDS elemental analysis results from two points of (a) A and (b) B on the fracture surface of failed dissimilar weldment.

environment can affect the chemical composition of the IMC layer at the interface and subsequent phase transformations, as well, by controlling the diffusion of elements during UFSW treatment as a function of w/v ratio. The chemical composition of the IMC layer determined as a complex phase between Fe, Al, and Mg elements. In this regard, the chemical composition of the IMC layer for all processed Samples I to XII is characterized by EDS analysis and expressed in Table 4. Based on such analysis results, by changing them into the atomic percent ratios and considering the minor amount of magnesium element, the formation of the $FeAl_2$ IMC phase seems more probable.

4.5. *Tensile flow behavior of dissimilar weldments and the related fractographic aspects*

Fig. 10a shows the force-displacement graph up to the failure point for two dissimilar weldments processed under two UFSW parameters of $w = 2000$ rpm/$v = 40$ mm/min and $w = 1600$ rpm/$v = 40$ mm/min, i.e., in the case of Samples X and VII. As seen, by increasing the heat input ratio and growth of IMC layer, the peak force point is reduced due to more brittleness of dissimilar weldment across the interface, although, the joint elongation to failure increased oppositely due to more microstructural changing and formation of a thicker HAZ area. The concave parts of the force-displacement curves in Fig. 10(a) can be attributed to the changes in the path of crack propagation along with the Al/Fe interface. Drops in loading curves are due to the cleavage part of the tensile-shear fracture and passing the cracks along with the IMC layer at the interface. Variation of the ultimate tensile strength (UTS) for all processed dissimilar weldments under UFSW condition are plotted versus the rotational speed at different traverse velocities of tool in Fig. 10(b). As shown, for all v, the UTS is increased at first by increasing w from 950 rpm up to 1650 rpm, and after that reduced by more increasing w up to 2000 rpm. On the other side, at a constant w, by reducing v, the UTS is continuously improved. As the main result, the most reli-

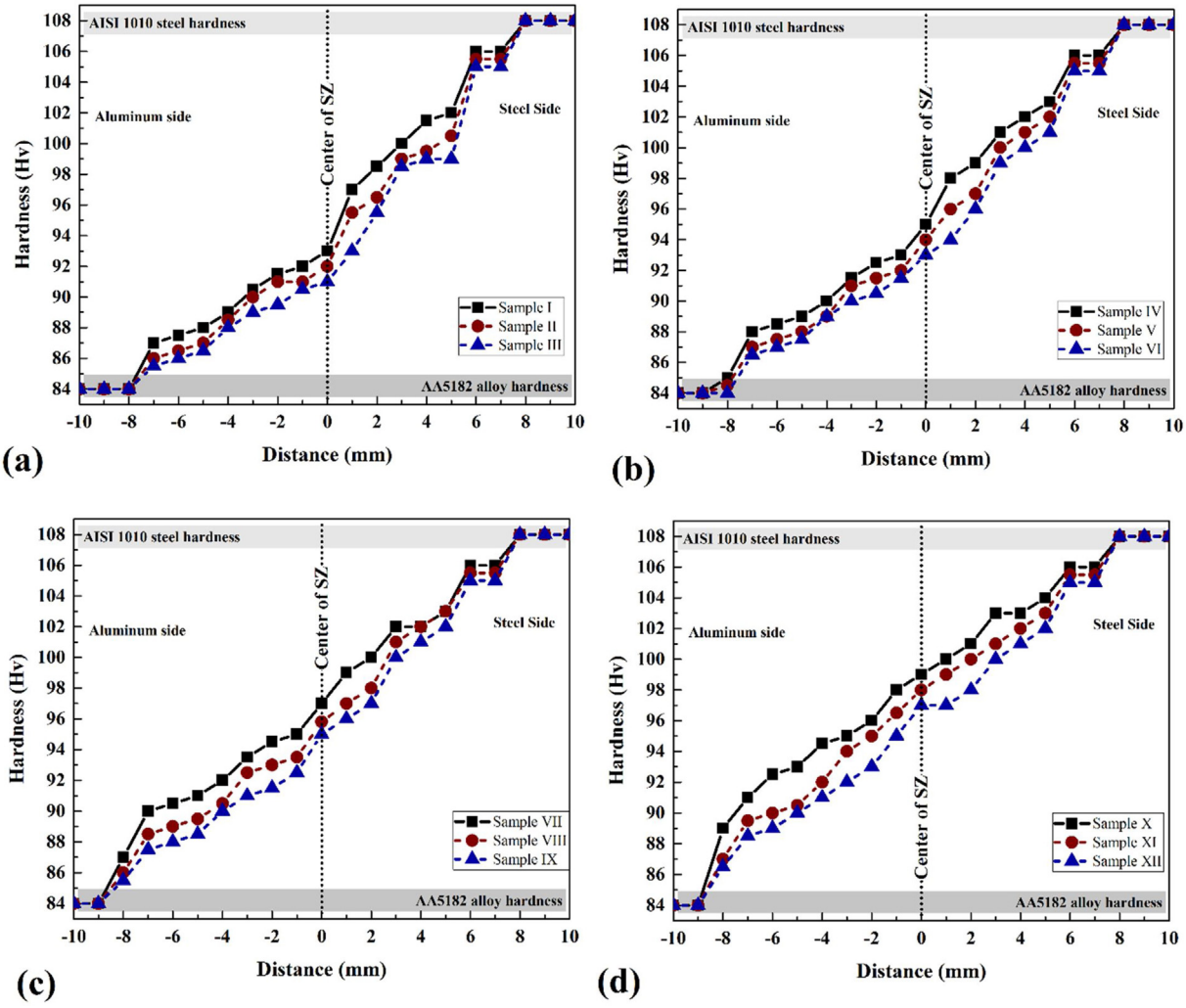

Fig. 12 – Micro-hardness profiles across dissimilar weldments for different rotational speeds of (a) 950, (b) 1300, (c) 1650, and (d) 1200 rpm during the UFSW process.

able dissimilar joint with the highest UTS value of ~80 MPa is attained at a moderate UFSW condition with optimized parameters as $w = 1650$ rpm and $v = 40$ mm/min, i.e., Sample VII. Accordingly, a maximum joining efficiency of ~30% can be noted for processed dissimilar weldments by the UFSW route. It is worth mentioning that for all prepared dissimilar weldments under the submerged processing conditions, the failure location was across the Al/Fe interface. Meanwhile, different features were revealed on the fracture surfaces considering the fractographic studies, depending on the implemented underwater FSW parameters. FE-SEM fractography from the related fracture surface for this optimized Sample VII are demonstrated in Fig. 10(c–e). By analysis these fractographs, a combined ductile-brittle fracture mechanism can be stated for this dissimilar weldment, whereas the contribution of ductile mode is not significant by less formation of dimples on the fracture surfaces. The EDS point scan analysis results from white contrast features on the fracture surface, as addressed by points A and B on FE-SEM images are illustrated in Fig. 11(a and b), respectively, which can approve the presence of IMC particles on the surface and contribution of the IMC layer on the brittle failure behavior of dissimilar weldments.

4.6. *Micro-hardness profiles*

Results for indentation Vickers micro-hardness profiles across the thickness section of dissimilar weldments versus the distance are plotted for different Samples of I to XII in Fig. 12(a–d) from the center of SZ for both aluminum and steel sides. As distinct, all hardness profiles exhibit a nonsymmetrical trend due to different physical and mechanical properties of dissimilar base materials in advancing and retreating sides. For all dissimilar weldments, the indentation hardness is continuously increased from the aluminum side to the steel one. In general, the alteration of hardness profiles by changing the UFSW processing parameters is not significant. The only issue is the hardness values close to the SZ centerline, which is considerably affected by the submerged cooling medium caused by the modification of microstructure due to rapid cooling. As shown, from Sample I toward Sample XII or from Fig. 12(a–d), i.e., by increasing w and decreasing v or increasing the heat input index in terms of w/v ratio, the hardness of SZ is continuously increased. In the competition between two opposite effects, the variations of hardness profiles can be discussed, as

changes in the grain size and formation of intermetallic compounds layer. As explained before, by referring to the grain size distribution plots of Fig. 7 as a function of rotational speed and traverse velocity of tool, under different processing conditions of UFSW treatment, the alteration of average grain size was not significant. But, on the other side, by increasing the heat input ratio, the formation and growth of the IMC layer at the interface can proceed during the UFSW process. Based on the observed increasing trend of hardness by increasing the heat input index, it seems that the second phenomenon regarding the contribution of the IMC layer is dominant. By comparing the different processing conditions, it can found that the fragmentation of steel part and a higher percentage of IMC particles under high heat input of UFSW treatment induced a higher hardness in the SZ.

5. Conclusions

This article focused on the first time on numerical modeling of underwater friction-stir welding (FSW) as an alternate joining route for dissimilar bonding of aluminum and steel alloys in a butt-joint design by controlling the operative metallurgical phenomena. An advanced 3D volume of fluid (VOF) model was used for this purpose. Besides, the effects of UFSW processing parameters on the microstructural details and mechanical property of dissimilar weldments were addressed by experimental studies, as well. According to the simulation results, thermal history, materials flow, and intermixing largely affected by the main processing parameters in terms of tool rotational speed (950−2000 rpm) and traverse velocity (40−100 mm/min), those can control the mechanical interlocking, formation of IMC layer at the Al/St interface, and grain structural evolution in the weld nugget. Increasing w and decreasing v in the submerged underwater atmosphere led continuous increasing of peak temperature up to 623 K and 773 K for the aluminum and steel sides, respectively, showed a good agreement with the experimental results. In both aluminum and steel sides of dissimilar weld nugget, the grain size was considerably refined down to <4 μm and 12 μm, respectively, with a continuous trend by increasing w and decreasing v. Accordingly, the thickness of IMC layer at the interface was increased for the upper and lower regions of dissimilar weld nugget up to ~5 μm and 1 μm, respectively, depending on the amount of heat input. All dissimilar weldments were failed from the Al/St interface varied by changing the thickness of the IMC layer. Implementation of a moderate UFSW condition with $w = 1650$ rpm and $v = 40$ mm/min imparted the highest joint mechanical strength of ~80 MPa with a joining efficiency of ~30%.

Conflict of interest

The authors declare that they have no known competing financial interests or personal relationships that could have appeared to influence the work reported in this paper.

Appendix A. Supplementary data

Supplementary material related to this article can be found, in the online version, at doi:https://doi.org/10.1016/j.jmrt.2020.02.003.

REFERENCES

[1] Aghajani Derazkola H, Elyasi M, Hossienzadeh M. Effects of friction stir welding tool plunge depth on microstructure and texture evolution of AA1100 to A441 AISI joint. ADMT J 2016;9(1).

[2] Elyasi M, Aghajani Derazkola H, Hosseinzadeh M. Investigations of tool tilt angle on properties friction stir welding of A441 AISI to AA1100 aluminium. Proc Inst Mech Eng Part B J Eng Manuf 2016;230(7):1234–41.

[3] Elyasi M, Aghajani H, Hosseinzadeh M. Effects of friction stir welding parameters on mechanical quality of AA1100 aluminum alloy to A441 AISI steel joint. mdrsjrns 2015;15(4):379–90.

[4] Elyasi M, Aghajani H, Hossinzadeh M. Study on joint zone microstructure evolution and hardness in friction stir welding of AA1100 aluminum alloy to A441 AISI steel. mdrsjrns 2015;14(14):97–107.

[5] Khodabakhshi F, Ghasemi Yazdabadi H, Kokabi AH, Simchi A. Friction stir welding of a P/M Al-Al_2O_3 nanocomposite: microstructure and mechanical properties. Mater Sci Eng A 2013;585:222–32.

[6] Khodabakhshi F, Haghshenas M, Chen J, Shalchi Amirkhiz B, Li J, Gerlich A. Bonding mechanism and interface characterisation during dissimilar friction stir welding of an aluminium/polymer bi-material joint. Sci Technol Weld Joining 2017;22(3):182–90.

[7] Khodabakhshi F, Haghshenas M, Sahraeinejad S, Chen J, Shalchi B, Li J, et al. Microstructure-property characterization of a friction-stir welded joint between AA5059 aluminum alloy and high density polyethylene. Mater Charact 2014;98:73–82.

[8] Khodabakhshi F, Simchi A, Kokabi AH, Gerlich AP. Similar and dissimilar friction-stir welding of an PM aluminum-matrix hybrid nanocomposite and commercial pure aluminum: microstructure and mechanical properties. Mater Sci Eng A 2016;666:225–37.

[9] Khodabakhshi F, Simchi A, Kokabi AH, Gerlich AP, Nosko M, Švec P. Influence of hard inclusions on microstructural characteristics and textural components during dissimilar friction-stir welding of an PM Al–Al_2O_3–SiC hybrid nanocomposite with AA1050 alloy. Sci Technol Weld Joining 2017;22(5):412–27.

[10] Derazkola HA, Khodabakhshi F. A novel fed friction-stir (FFS) technology for nanocomposite joining. Sci Technol Weld Joining 2019:1–12.

[11] Haghshenas M, Khodabakhshi F. Dissimilar friction-stir welding of aluminum and polymer: a review. Int J Adv Manuf Technol 2019;104(1):333–58.

[12] Derazkola HA, Aval HJ, Elyasi M. Analysis of process parameters effects on dissimilar friction stir welding of AA1100 and A441 AISI steel. Sci Technol Weld Joining 2015;20(7):553–62.

[13] Aghajani Derazkola H, Khodabakhshi F. Intermetallic compounds (IMCs) formation during dissimilar friction-stir welding of AA5005 aluminum alloy to St-52 steel: numerical modeling and experimental study. Int J Adv Manuf Technol 2019;100(9):2401–22.

[14] Khodabakhshi F, Gerlich AP, Simchi A, Kokabi AH. Cryogenic friction-stir processing of ultrafine-grained Al-Mg-TiO_2 nanocomposites. Mater Sci Eng A 2014;620:471–82.
[15] Derazkola HA, Khodabakhshi F. Underwater submerged dissimilar friction-stir welding of AA5083 aluminum alloy and A441 AISI steel. Int J Adv Manuf Technol 2019;102(9):4383–95.
[16] Khodabakhshi F, Marzbanrad B, Shah LH, Jahed H, Gerlich AP. Friction-stir processing of a cold sprayed AA7075 coating layer on the AZ31B substrate: structural homogeneity, microstructures and hardness. Surf Coat Technol 2017;331 Supplement C:116–28.
[17] Mishra RS, Ma ZY. Friction stir welding and processing. Mater Sci Eng 2005;R50(1–2):1–78.
[18] Xue P, Xiao BL, Ma ZY. Achieving large-area bulk ultrafine grained Cu via submerged multiple-pass friction stir processing. J Mater Sci Technol 2013;29(12):1111–5.
[19] Khodabakhshi F, Nosko M, Gerlich AP. Effects of graphene nano-platelets (GNPs) on the microstructural characteristics and textural development of an Al-Mg alloy during friction-stir processing. Surf Coat Technol 2018;335:288–305.
[20] Khodabakhshi F, Nosko M, Gerlich AP. Dynamic restoration and crystallographic texture of a friction-stir processed Al–Mg–SiC surface nanocomposite. Mater Sci Technol 2018;34(14):1773–91.
[21] KHODABAKHSHI F, NOSKO M, GERLICH AP. Influence of CNTs decomposition during reactive friction-stir processing of an Al–Mg alloy on the correlation between microstructural characteristics and microtextural components. J Microscopy 2018;271(2):188–206.
[22] Liu HJ, Zhang HJ, Yu L. Homogeneity of mechanical properties of underwater friction stir welded 2219-T6 aluminum alloy. J Mater Eng Perform 2011;20(8):1419–22.
[23] Liu HJ, Zhang HJ, Yu L. Effect of welding speed on microstructures and mechanical properties of underwater friction stir welded 2219 aluminum alloy. Mater Des 2011;32(3):1548–53.
[24] Liu HJ, Zhang HJ, Huang YX, Yu L. Mechanical properties of underwater friction stir welded 2219 aluminum alloy. Trans Nonferrous Met Soc China 2010;20(8):1387–91.
[25] Zhang H, Liu H. Characteristics and formation mechanisms of welding defects in underwater friction stir welded aluminum alloy. Metallogr Microstruct Anal 2012;1(6):269–81.
[26] Zhang H, Liu H. Mathematical model and optimization for underwater friction stir welding of a heat-treatable aluminum alloy. Mater Des 2013;45:206–11.
[27] Zhang HJ, Liu HJ, Yu L. Effect of water cooling on the performances of friction stir welding heat-affected zone. J Mater Eng Perform 2012;21(7):1182–7.
[28] Zhang HJ, Liu HJ, Yu L. Microstructure and mechanical properties as a function of rotation speed in underwater friction stir welded aluminum alloy joints. Mater Des 2011;32(8):4402–7.
[29] Zhang HJ, Liu HJ, Yu L. Microstructural evolution and its effect on mechanical performance of joint in underwater friction stir welded 2219-T6 aluminium alloy. Sci Technol Weld Joining 2011;16(5):459–64.
[30] Sabari SS, Malarvizhi S, Balasubramanian V. The effect of pin profiles on the microstructure and mechanical properties of underwater friction stir welded AA2519-T87 aluminium alloy. Int J Mech Mater Eng 2016;11(1):5.
[31] Sree Sabari S, Malarvizhi S, Balasubramanian V, Madusudhan Reddy G. Experimental and numerical investigation on under-water friction stir welding of armour grade AA2519-T87 aluminium alloy. Def Technol 2016;12(4):324–33.
[32] Heirani F, Abbasi A, Ardestani M. Effects of processing parameters on microstructure and mechanical behaviors of underwater friction stir welding of Al5083 alloy. J Manuf Processes 2017;25:77–84.
[33] Liang H, Yan K, Wang Q, Zhao Y, Liu C, Zhang H. Improvement in joint strength of spray-deposited Al-Zn-Mg-Cu alloy in underwater friction stir welding by altered temperature of cooling water. J Mater Eng Perform 2016;25(12):5486–93.
[34] Wang Q, Zhao Z, Zhao Y, Yan K, Liu C, Zhang H. The strengthening mechanism of spray forming Al-Zn-Mg-Cu alloy by underwater friction stir welding. Mater Des 2016;102:91–9.
[35] Wang Q, Zhao Z, Zhao Y, Yan K, Zhang H. The adjustment strategy of welding parameters for spray formed 7055 aluminum alloy underwater friction stir welding joint. Mater Des 2015;88:1366–76.
[36] Papahn H, Bahemmat P, Haghpanahi M, Sommitsch C. Study on governing parameters of thermal history during underwater friction stir welding. Int J Adv Manuf Technol 2015;78(5):1101–11.
[37] Tan YB, Wang XM, Ma M, Zhang JX, Liu WC, Fu RD, et al. A study on microstructure and mechanical properties of AA 3003 aluminum alloy joints by underwater friction stir welding. Mater Charact 2017;127:41–52.
[38] Zhao Y, Lu Z, Yan K, Huang L. Microstructural characterizations and mechanical properties in underwater friction stir welding of aluminum and magnesium dissimilar alloys. Mater Des 2015;65:675–81 (1980-2015).
[39] Zhao Y, Jiang S, Yang S, Lu Z, Yan K. Influence of cooling conditions on joint properties and microstructures of aluminum and magnesium dissimilar alloys by friction stir welding. Int J Adv Manuf Technol 2016;83(1):673–9.
[40] Zhang J, Shen Y, Yao X, Xu H, Li B. Investigation on dissimilar underwater friction stir lap welding of 6061-T6 aluminum alloy to pure copper. Mater Des 2014;64:74–80.
[41] Mahto RP, Gupta C, Kinjawadekar M, Meena A, Pal SK. Weldability of AA6061-T6 and AISI 304 by underwater friction stir welding. J Manuf Processes 2019;38:370–86.
[42] Sadeghian B, Taherizadeh A, Atapour M. Simulation of weld morphology during friction stir welding of aluminum-stainless steel joint. J Mater Process Technol 2018;259:96–108.
[43] Khodabakhshi F, Gerlich AP, Simchi A, Kokabi AH. Cryogenic friction-stir processing of ultrafine-grained Al–Mg–TiO_2 nanocomposites. Mater Sci Eng A 2015;620:471–82.
[44] Khodabakhshi F, Nosko M, Gerlich AP. Dynamic restoration and crystallographic texture of a friction-stir processed Al–Mg–SiC surface nanocomposite. Mater Sci Technol (United Kingdom) 2018;34(14):1773–91.
[45] McNelley TR, Swaminathan S, Su JQ. Recrystallization mechanisms during friction stir welding/processing of aluminum alloys. Scr Mater 2008;58(5):349–54.
[46] Derazkola HA, Khodabakhshi F. A novel fed friction-stir (FFS) technology for nanocomposite joining. Sci Technol Weld Joining 2020;25(2):89–100.
[47] Hernández CA, Ferrer VH, Mancilla JE, Martínez LC. Three-dimensional numerical modeling of the friction stir welding of dissimilar steels. Int J Adv Manuf Technol 2017;93(5):1567–81.
[48] Gale WF, Totemeier TC. In: Smithells Metals Reference Book. Elsevier Science; 2003.
[49] Derazkola HA, Khodabakhshi F, Simchi A. Friction-stir lap-joining of aluminium-magnesium/poly-methyl-methacrylate hybrid structures: thermo-mechanical modelling and experimental feasibility study. Sci Technol Weld Joining 2018;23(1):35–49.